Analytical Method Using Virtual PM Blocks to Represent Magnet Segmentations in Surface-Mounted PM Synchronous Machines

Tow Leong Tiang[1], Dahaman Ishak[2, *], Chee Peng Lim[3], and Mohd Rezal[2]

Abstract—This paper describes an analytical subdomain model to predict the magnetic field distributions in the semi-closed surface-mounted permanent magnet synchronous machines (PMSMs) due to magnet segmentations with radial magnetization (RM). The magnet segments per pole can be virtually represented by finite number of permanent magnet (PM) blocks and Fourier decompositions. The model can also determine the optimum magnet pole-arcs for each segment and the optimum airgap spacing between the segments. The analytical model is then applied to evaluate the performance of a three-phase, 12-slot/8-pole, surface-mounted PMSM having two segmented magnets per pole with RM. With design objective for minimum cogging torque and minimum total harmonic distortion in phase back-emf waveforms, we obtain that the optimum settings are 147.6° elect. for magnet segment pole-arc and 11.2° elect. for airgap spacing between the magnet segments. These analytical results are further compared and validated by 2-D finite element analysis (FEA). Additionally, we also compare the results with those from the optimum magnet pole-arc of one magnet segment per pole machine. It is observed that the cogging torque and total harmonic distortion THD_v of the phase back-EMF are significantly reduced by 89% and 25%, respectively, with constraint and assumption that both machines utilize similar total magnet volume.

1. INTRODUCTION

The improvement and innovation in the rare-earth magnetic materials have accelerated their use in electrical machines. These magnetic materials which have very high energy product created opportunity for various machine topologies and complexity in the design and construction of permanent magnet (PM) AC motors such as surface-mounted PMSM, inset PMSM, and interior PMSM for either internal rotor structure or external rotor structure. Compared with the conventional electrical machines, PMSMs are very popular in aviation industries, electric propulsion, servo drives and renewable energy technologies since PMSMs exhibit higher efficiency, higher torque density, compact size, excellent dynamic performance, and almost maintenance free [1, 2]. However, the drawbacks of PMSMs are the unwanted noise and vibration which can originate from the motor torque ripples [3, 4].

Torque ripples in PMSMs, in general, can be attributed to several reasons such as [5]: (i) cogging torque due to the magnetic attraction or magnetic forces between the stator slot openings and the rotor magnets; (ii) higher order harmonics in the induced phase back-EMF; (iii) nonlinear property of the stator and rotor cores; and (iv) higher order harmonics in the motor currents from inverter switching. Many researches have been devoted to mitigate or minimize the torque ripples in PMSMs by employing several techniques such as using fractional slot-to-pole number, dummy slots on stator pole surface, magnet pole-arcs, magnet stepping, stator skewing, rotor skewing, different magnetization patterns in rotor magnets, and shifting the magnet poles [6].

[1] Universiti Malaysia Perlis, Pauh Putra Campus, Arau, Perlis 02600, Malaysia. [2] Universiti Sains Malaysia, Engineering Campus, NibongTebal, Penang 14300, Malaysia. [3] Deakin University, Geelong Waurn Ponds Campus, Geelong, Victoria 3220, Australia.

However, the use of magnet segmentations per pole in the rotor for the sole purpose of reducing the cogging torque and harmonics in the induced phase back-EMF in surface-mounted PMSMs is still not yet comprehensively researched and documented. On the contrary, the concept of magnet segmentation was first deployed to minimize the eddy current losses in PM mounted on the rotor surface which can be significantly reduced by splitting or segmenting the magnet into smaller pieces, either axially or circumferentially. For example, the problem of rotor losses from the circumferential segmented magnets in surface-mounted PMSMs was investigated: (i) rotor losses due to eddy currents in uniform segmented magnets [7] and in non-uniform segmented magnets [8]; (ii) optimization of segmented magnets for minimum rotor eddy current losses [9].

Previous researches have attempted to address the cogging torque minimization issue via magnet segmentation technique. For instance, the authors in [10] used Fourier series to estimate the harmonics of cogging torque originating from the segmented magnet blocks per rotor pole. Appropriate magnet span and optimum location of magnet blocks were then calculated based on the outcomes of empirical formulae which might suppress the fundamental harmonic of cogging torque waveform. Reducing the cogging torque in surface-mounted PMSMs by optimizing the magnet segments based on semi-analytical model coupled with an airgap permeance function was proposed in [11]. Meanwhile, the authors in [12] applied three optimization tools to determine the optimum spans of magnet segments. Here, energy method in semi-analytical model was used to evaluate the cogging torque in open-slotted surface-mounted PMSM. Nevertheless, the calculated cogging torque is arguably less accurate because the model did not consider the energy coming from the tangential component of magnetic fields in the slot openings.

In this paper, multiple magnet segmentations with radial magnetization (RM) per rotor pole are first formulated using superposition concept from a finite number of PM blocks. The Fourier decompositions that describe the magnetization vectors from each PM block are then incorporated into the exact 2-D analytical subdomain model in order to predict the magnetic field distributions in the regions of PM, airgap, slot openings and winding slots, respectively. The exact 2-D analytical subdomain model which is reasonably fast and accurate is often preferred during the initial design stage of PM machines in order to predict motor global quantities [13–17]. In this paper, we will show that our analytical subdomain model of segmented magnets with RM per pole in the 2-D semi-closed surface-mounted PMSMs constructed from virtual PM blocks can also account for the influence of stator slotting and tooth-tips. The motor global quantities in PMSMs such as the phase back-EMF, cogging torque, and total harmonic distortion (THD_v) are computed. Optimum segmented magnet pole arcs for each segment are also evaluated for minimum cogging torque and minimum THD_v. The analytical model is applied on a three-phase, $12\,s/8\,p$ semi-closed surface-mounted PMSM. Then, the analytical results are compared with those obtained from 2-D finite element analysis (FEA) for validation purpose.

2. MACHINE SPECIFICATIONS AND ASSUMPTIONS

A typical layout of a three-phase, surface-mounted PMSM with segmented magnets per rotor pole is shown in Figure 1 where all symbols and regions are clearly indicated. In formulating the exact 2-D analytical subdomain model, important assumptions for deriving the model pertaining to the segmented magnets are [13]: (a) effect of induced eddy current is ignored; (b) actual relative permeability in PMs is considered; (c) stator and rotor laminations are non-conductive; (d) linear BH curve for PMs; (e) sides of stator slots are radially extended; (f) end effects of PM machines are ignored; (g) stator and rotor laminations are infinitely permeable; and (h) only z-component of magnetic vector potential exists in 2-D polar coordinates, and it is determined by the radial position r, and tangential position α. The derived analytical subdomain model is evaluated on a three-phase, surface-mounted PMSM whose parameters and dimensions are given in Table 1.

3. VIRTUAL PM BLOCKS TO REPRESENT MAGNET SEGMENTATIONS

While different magnetization patterns and modeling techniques are available in the literature [14, 15], the segmented magnets in each magnetic pole can also be graphically represented by Figure 2. Hypothetically, the segmented magnets per pole can be formulated such that the net magnetic flux is
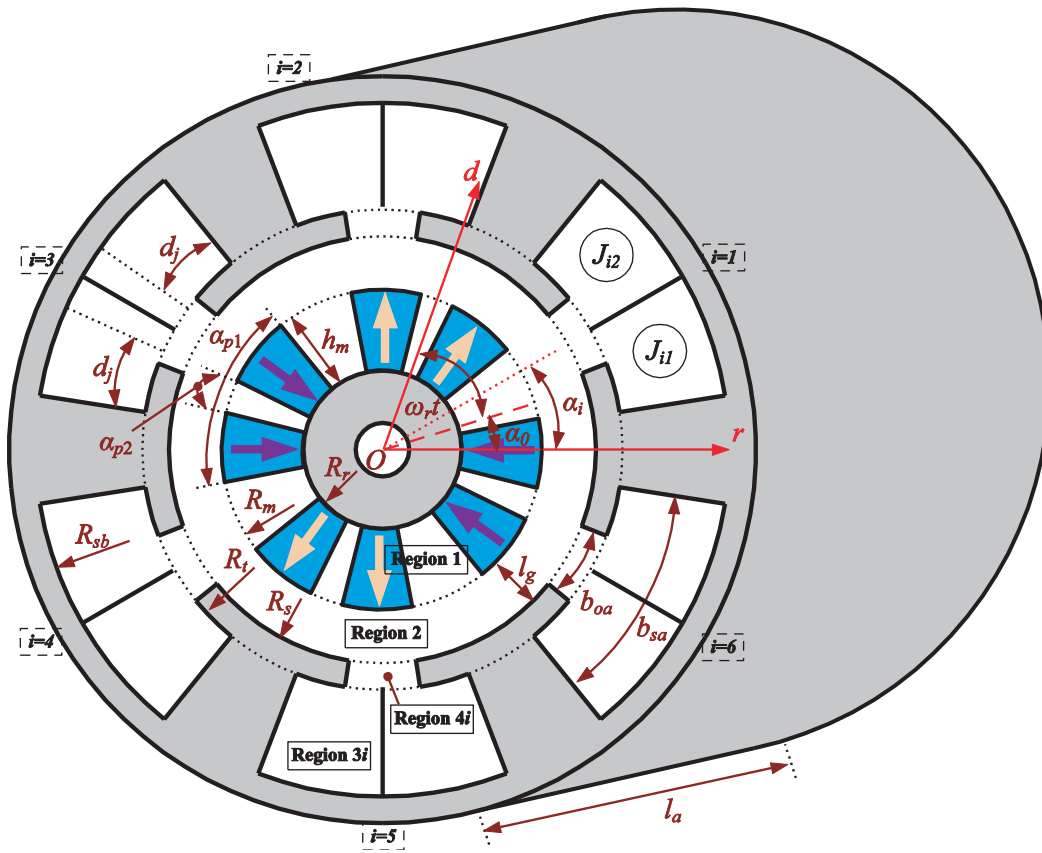
Figure 1. Typical geometry of a surface-mounted PMSM with two segmented magnets per rotor pole.

Table 1. Specifications and dimensions for 12 s/8 p PMSMs.

|			
Slot number, N_s	12	Winding turns/coil, N_c	30
Pole number, $2p$	8	Stator inner diameter	54 mm
Stator outer diameter	100 mm	Tooth-tips edge	3 mm
Remanence, B_r	1.12 T	Slot-opening angle, b_{oa}	5.5° mech
Active length, l_a	50 mm	Winding slot angle, b_{sa}	15° mech
Airgap length, l_g	1 mm	Stator yoke height	7.5 mm
Magnet thickness, h_m	3 mm	Rotor outer diameter	52 mm
Relative recoil permeability, μ_r	1.05	Rotor yoke inner radius, R_r	23 mm
PM surface radius, R_m	26 mm	Magnetization pattern	RM
Slot-openings inner radius, R_s	27 mm	Slot-openings outer radius, R_t	30 mm
Bottom slots radius, R_{sb}	42.5 mm	Optimum magnet pole-arc per pole of 1st virtual PM block for 2 SM machine, α_{p1}	147.6° elect.
Optimum magnet pole-arc per pole for 1 SM machine	136.4° elect.	Optimum magnet pole-arc per pole of 2nd virtual PM block for 2 SM machine, α_{p2}	11.2° elect.
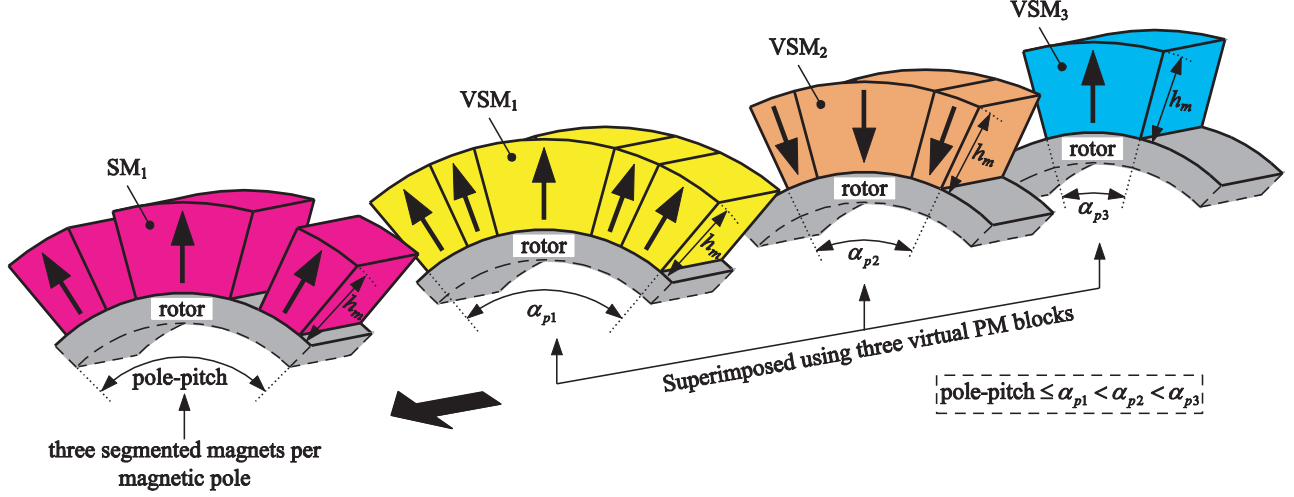
Figure 2. Representation of three segmented magnets per rotor pole by three superimposed virtual PM blocks with same magnet thickness and located on common rotor surface of PMSM.

achieved by summation of individual flux from the virtual PM blocks, which are having the same magnet thickness located on the rotor surface. As shown in Figure 2, the effect of three segmented magnets can be constructed from a group of three virtual PM blocks that are superimposed together axially. Any regions meant to cancel out each other have identical surface area (for the 2D model) or identical volume (for a 3D model). The blocks are mounted on the rotor surface with common circumferential radii and same magnet thickness h_m, but the blocks comes with different pole arcs following this rule: pole-pitch $\leq \alpha_{p1} < \alpha_{p2} < \alpha_{p3} < \ldots < \alpha_{pv}$, where v is the number of segmented magnet. The polarities of virtual PM blocks VSM$_1$, VSM$_2$, and VSM$_3$ are alternate, which are represented by either positive or negative signs governed by $(-1)^{(v+1)}$ from (9). Since the PM blocks VSM$_1$, VSM$_2$, and VSM$_3$ are isotropic and homogenous with similar relative permeability and remanence, the magnitude of magnetic moments in each virtual segmented magnet is also the same. These virtual magnet segments are directly summed up or cancelled out through its polarities to obtain the net magnetic flux of the segmented magnet, SM$_1$, as shown in Figure 2. Three virtual PM blocks are superimposed to build three segmented magnets per rotor pole. Therefore, similar number of virtual PM blocks are required to be superimposed in order to realize the similar number of segmented magnets per rotor pole.

Different pole-arc ratios of two virtual PM blocks with opposite magnetization directions create the gap between the PMs. Estimating and optimizing the pole-arcs of the vth virtual PM blocks, i.e., α_{p1}, α_{p2}, $\alpha_{p3}, \ldots, \alpha_{pv}$ can provide the optimum settings for each magnet segment and the airgap spacing between magnet segments per rotor pole. Since Fourier decompositions of magnetic fluxes from each virtual PM block can be applied, the net magnetic flux density from the segmented magnets per pole can be obtained. Therefore, the magnetization patterns of the segmented magnets per pole can be expressed in Fourier Series with radial magnetization (RM) patterns as

$$M_r = \sum_{k=up=1,3,5,\ldots} M_{rk} \cos\left(k\alpha - k\omega_r t - k\alpha_0\right) \tag{1}$$

$$= \sum_{k=up=1,3,5,\ldots} M_{rck} \cos\left(k\alpha\right) + M_{rsk} \sin\left(k\alpha\right) \tag{2}$$

$$M_\alpha = \sum_{k=up=1,3,5,\ldots} M_{\alpha k} \sin\left(k\alpha - k\omega_r t - k\alpha_0\right) \tag{3}$$

$$= \sum_{k=up=1,3,5,\ldots} M_{\alpha ck} \cos\left(k\alpha\right) + M_{\alpha sk} \sin\left(k\alpha\right) \tag{4}$$

$$M_{rck} = M_{rk} \cos(k\omega_r t + k\alpha_0) \tag{5}$$

$$M_{rsk} = M_{rk} \sin(k\omega_r t + k\alpha_0) \tag{6}$$

$$M_{\alpha ck} = M_{\alpha k} \sin(k\omega_r t + k\alpha_0) \tag{7}$$

$$M_{\alpha sk} = M_{\alpha k} \cos(k\omega_r t + k\alpha_0) \tag{8}$$

where

$$M_{rk} = \sum_{\substack{v = 1, 2, 3, \dots \\ k/p = 1, 3, 5, \dots}} (-1)^{(v+1)} \, 4pB_r \sin\left(k\pi\alpha_{pv}/2p\right) \Big/ k\pi\mu_0 \tag{9}$$

$$M_{\alpha k} = 0 \tag{10}$$

where M_r and M_α are the normal and circumferential components of magnet magnetization; u is the harmonic number of PM; p is the number of pole-pair; α_0 is the rotor position at initial location; ω_r is the angular speed of the rotor; B_r is the remanence of PM; α_{pv} is the ratio of magnetic pole span of v-pieces of the virtual PM blocks; M_{rk} and $M_{\alpha k}$ are the normal and circumferential components of magnetization vector with kth harmonic number. From here, Laplace's and Poisson's equations are solved by using separation of variables technique to obtain the magnetic field solutions in each subdomain [18].

3.1. Vector Magnetic Potential and Current Density Profile

The vector potentials in Region 1 (A_{z1}) for PMs, Region 2 (A_{z2}) for the airgap, Region $3i$ (A_{z3i}) for the winding slots, and Region $4i$ (A_{z4i}) for the slot openings are governed by

$$\frac{\partial^2 A_{z1}}{\partial r^2} + \frac{1}{r}\frac{\partial A_{z1}}{\partial r} + \frac{1}{r^2}\frac{\partial^2 A_{z1}}{\partial \alpha^2} = -\frac{\mu_0}{r}\left(M_\alpha - \frac{\partial M_r}{\partial \alpha}\right) \tag{11}$$

$$\frac{\partial^2 A_{z2}}{\partial r^2} + \frac{1}{r}\frac{\partial A_{z2}}{\partial r} + \frac{1}{r^2}\frac{\partial^2 A_{z2}}{\partial \alpha^2} = 0 \tag{12}$$

$$\frac{\partial^2 A_{z3i}}{\partial r^2} + \frac{1}{r}\frac{\partial A_{z3i}}{\partial r} + \frac{1}{r^2}\frac{\partial^2 A_{z3i}}{\partial \alpha^2} = -\mu_0 J \tag{13}$$

$$\frac{\partial^2 A_{z4i}}{\partial r^2} + \frac{1}{r}\frac{\partial A_{z4i}}{\partial r} + \frac{1}{r^2}\frac{\partial^2 A_{z4i}}{\partial \alpha^2} = 0 \tag{14}$$

where J is the current density. Figure 3 shows the current density profile of a slot area, which can be expressed as

$$J = J_{i0} + \sum_n J_{in} \cos\left[E_n\left(\alpha + b_{sa}/2 - \alpha_i\right)\right], \quad \text{for} \quad \alpha_i - b_{sa}/2 \leq \alpha \leq \alpha_i + b_{sa}/2 \tag{15}$$

$$J_{i0} = \left(J_{i1} + J_{i2}\right) d_j/b_{sa} \tag{16}$$

$$J_{in} = \left[2\left(J_{i1} + J_{i2}\cos n\pi\right)\sin\left(n\pi d_j/b_{sa}\right)\right]/n\pi \tag{17}$$

$$E_n = n\pi/b_{sa} \tag{18}$$

where n is the harmonic number in the winding slot, d_j the width angle of slot area with J_i excitation current density, and α_i the ith slot rotor position.
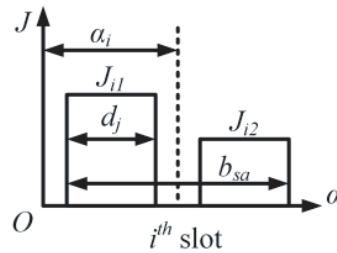

Figure 3. Profile of current density J_i in slot area.

The vector magnetic potential distribution in the PM region can be expressed by

$$A_{z1} = \sum_k \left[\left(C_{1k}A_1 + C_{2k}M_{\alpha ck} - C_{3k}M_{rsk}\right)\cos\left(k\alpha\right) + \left(C_{1k}C_1 + C_{2k}M_{\alpha sk} + C_{3k}M_{rck}\right)\sin\left(k\alpha\right)\right] \tag{19}$$

where

$$C_{1k} = \left(r/R_m\right)^k + G_1\left(r/R_r\right)^{-k} \tag{20}$$

$$C_{2k} = \begin{cases} \mu_0 \left[R_r k \, (r/R_r)^{-k} + r \right] \Big/ (k^2 - 1), & k \neq 1 \\ \mu_0 \left[2R_r \, (r/R_r)^{-1} + r \right], & k = 1 \end{cases} \tag{21}$$

$$C_{3k} = \begin{cases} \mu_0 \left[R_r \, (r/R_r)^{-k} + kr \right] \Big/ (k^2 - 1), & k \neq 1 \\ \mu_0 \left[R_r \, (r/R_r)^{-1} + r \right], & k = 1 \end{cases} \tag{22}$$

$$G_1 = (R_r/R_m)^k \tag{23}$$

On the other hand, the general field distribution in the airgap is given by

$$A_{z2} = \sum_k \left\{ \left[A_2 \, (r/R_s)^k + B_2 \, (r/R_m)^{-k} \right] \cos(k\alpha) + \left[C_2 \, (r/R_s)^k + D_2 \, (r/R_m)^{-k} \right] \sin(k\alpha) \right\} \tag{24}$$

Then, the general field solutions in Regions $3i$ and $4i$ can be obtained as

$$A_{z3i} = A_0 + \sum_n A_n \cos \left[E_n \left(\alpha + b_{sa}/2 - \alpha_i \right) \right] \tag{25}$$

$$A_{z4i} = D \ln r + Q_{4i} + \sum_m \left[C_{4i} \, (r/R_t)^{F_m} + D_{4i} \, (r/R_s)^{-F_m} \right] \cos \left[F_m \left(\alpha + b_{oa}/2 - \alpha_i \right) \right] \tag{26}$$

where

$$A_0 = \mu_0 J_{i0} \left(2R_{sb}^2 \ln r - r^2 \right) / 4 + Q_{3i} \tag{27}$$

$$A_n = D_{3i} \left[G_3 \, (r/R_{sb})^{E_n} + (r/R_t)^{-E_n} \right] + \mu_0 J_{in} \left[r^2 - 2R_{sb}^2 / E_n \, (r/R_{sb})^{E_n} \right] \Big/ \left(E_n^2 - 4 \right) \tag{28}$$

$$G_3 = (R_t/R_{sb})^{E_n} \tag{29}$$

$$F_m = m\pi/b_{oa} \tag{30}$$

where m is the harmonic number in slot-opening, and D is a constant. By imposing the continuity of interface conditions between regions in terms of flux density and vector potential, coefficients A_1, C_1, A_2, B_2, C_2, D_2, D_{3i}, Q_{3i}, C_{4i}, D_{4i}, Q_{4i}, and D in expressions (19), (24), and (25)–(28) can be obtained. A detailed computation can be found in Appendix.

3.2. Magnetic Flux Density

The normal and tangential components of flux density distributions are derived from the general vector potential expressions as

$$B_r = \partial A_z / (r \partial \alpha) \quad \text{and} \quad B_\alpha = -\partial A_z / \partial r \tag{31}$$

In PM region, the magnetic fluxes can be obtained by

$$\begin{aligned} B_{1r} = & -(1/r) \sum_k k \left(C_{1k} A_1 + C_{2k} M_{\alpha ck} - C_{3k} M_{rsk} \right) \sin(k\alpha) \\ & + (1/r) \sum_k k \left(C_{1k} C_1 + C_{2k} M_{\alpha sk} + C_{3k} M_{rck} \right) \cos(k\alpha) \end{aligned} \tag{32}$$

$$\begin{aligned} B_{1\alpha} = & -(1/r) \sum_k \left(C_{4k} A_1 + C_{5k} M_{\alpha ck} - C_{6k} M_{rsk} \right) \cos(k\alpha) \\ & - (1/r) \sum_k \left(C_{4k} C_1 + C_{5k} M_{\alpha sk} + C_{6k} M_{rck} \right) \sin(k\alpha) \end{aligned} \tag{33}$$

where

$$C_{4k} = k \left[(r/R_m)^k - G_1 \, (r/R_r)^{-k} \right] \tag{34}$$

$$C_{5k} = \begin{cases} \mu_0 \Big/ \left\{ (k^2 - 1) \left[-k^2 R_r \, (r/R_r)^{-k} + r \right] \right\}, & k \neq 1 \\ \mu_0 r \left[-2 \, (r/R_r)^{-2} + 1 \right], & k = 1 \end{cases} \tag{35}$$

$$C_{6k} = \begin{cases} \mu_0 k \Big/ \left\{ (k^2 - 1) \left[-R_r \, (r/R_r)^{-k} + r \right] \right\}, & k \neq 1 \\ \mu_0 r \left[- (r/R_r)^{-2} + 1 \right], & k = 1 \end{cases} \tag{36}$$

Similarly, for Region 2, the magnetic flux density of normal and tangential components in the airgap can be computed by

$$B_{2r} = \sum_k B_{rs} \sin(k\alpha) + \sum_k B_{rc} \cos(k\alpha) \tag{37}$$

$$B_{2\alpha} = \sum_k B_{\alpha c} \cos(k\alpha) + \sum_k B_{\alpha s} \sin(k\alpha) \tag{38}$$

where

$$B_{rs} = -k\left[A_2 (r/R_s)^k + B_2 (r/R_m)^{-k}\right]/r \tag{39}$$

$$B_{rc} = k\left[C_2 (r/R_s)^k + D_2 (r/R_m)^{-k}\right]/r \tag{40}$$

$$B_{\alpha c} = -k\left[A_2 (r/R_s)^k - B_2 (r/R_m)^{-k}\right]/r \tag{41}$$

$$B_{\alpha s} = -k\left[C_2 (r/R_s)^k - D_2 (r/R_m)^{-k}\right]/r \tag{42}$$

Lastly, for Regions 3 and 4 respectively, the magnetic flux densities in the copper slots of a non-overlapping machine and the slot-openings are given as the following

$$B_{rs} = -k\left[A_2 (r/R_s)^k + B_2 (r/R_m)^{-k}\right]/r \tag{43}$$

$$B_{rc} = k\left[C_2 (r/R_s)^k + D_2 (r/R_m)^{-k}\right]/r \tag{44}$$

$$B_{\alpha c} = -k\left[A_2 (r/R_s)^k - B_2 (r/R_m)^{-k}\right]/r \tag{45}$$

$$B_{\alpha s} = -k\left[C_2 (r/R_s)^k - D_2 (r/R_m)^{-k}\right]/r \tag{46}$$

4. PHASE BACK-EMF, COGGING TORQUE AND OPTIMUM SETTINGS

After formulating the field solutions, motor global quantities such as flux linkage, phase back-EMF and cogging torque are computed to evaluate further the motor performance. The flux linkage induced in a coil J_{i1} is obtained by

$$\psi_{i1} = (l_a N_c/A_c) \left\{ Z_0 d_j + \sum_n Z_n/[E_n \sin(E_n d_j)] \right\} \tag{47}$$

where A_c is the winding slot area of a coil, whereas the flux linkage induced in coil J_{i2} is attained by

$$\psi_{i2} = (l_a N_c/A_c) \left\{ Z_0 d_j - \sum_n Z_n/[E_n \sin(n\pi - E_n d_j)] \right\} \tag{48}$$

where

$$Z_0 = Q_{3i} \left(R_{sb}^2 - R_t^2\right)/2 + \mu_0 J_{i0} \left(\begin{array}{c} +4R_{sb}^4 \ln R_{sb} - 4R_{sb}^2 R_t^2 \ln R_t \\ -3R_{sb}^4 + 2R_{sb}^2 R_t^2 + R_t^4 \end{array} \right)/16 \tag{49}$$

$$Z_n = +D_{3i} G_3 \left(R_{sb}^2 - R_t^2 G_3\right)/(E_n + 2) + D_{3i} \left(R_t^2 - R_{sb}^2 G_3\right)/(E_n - 2)$$
$$+\mu_0 J_{in} \left(R_{sb}^4 - R_t^4\right)/\left[4\left(E_n^2 - 4\right)\right] + 2\mu_0 J_{in} R_{sb}^2 \left(R_t^2 G_3 - R_{sb}^2\right)/\left[E_n \left(E_n^2 - 4\right)\left(E_n + 2\right)\right] \tag{50}$$

The computation of total flux linkage in each phase is expressed by

$$\Psi_{abc} = S_w \psi_c \tag{51}$$

where S_w is the winding slots order and ψ_c is the phase flux linkage produced by each phase coils. Therefore, differentiating Eq. (51) with time yields the phase back-EMF as

$$E_{abc} = \omega_r d\Psi_{abc}/d\Delta \tag{52}$$

where Δ is the angular position of rotor. Furthermore, Fast-Fourier Transform is used to capture the THD_v of phase back-EMF, which can be calculated by

$$THD_v = \left(\sqrt{\sum_{x=2}^{\infty} V_x^2} \Big/ V_1 \right) \times 100 \tag{53}$$

where V_1 is the fundamental component of the phase back-EMF and V_x the higher order harmonics of phase back-EMF. Furthermore, Maxwell stress tensor is deployed to evaluate the cogging torque in the motor model as given by

$$T_c = \left(l_a r^2 / \mu_0\right) \int_0^{2\pi} B_{2r} B_{2\alpha} d\alpha \tag{54}$$

Therefore, the peak cogging torque can be estimated. The peak cogging torque and THD_v of the phase back-EMF are then normalized according to the feature scaling method as the following

$$y_{in} = \frac{y_i - \min(y)}{\max(y) - \min(y)} \tag{55}$$

where y_{in} is the normalized value of y_i, y_i the ith value of y, and y the data sample of either the peak cogging torque or THD_v of the phase back-EMF. Eventually, the optimum setting of magnet arcs required by the segmented magnets in any machines can be obtained.

5. RESULTS, DISCUSSION, AND FEA VALIDATION

The exact 2-D analytical subdomain model of segmented magnets per pole due to radial magnetization is further evaluated on a three-phase, surface-mounted PMSM to search for the optimum setting of magnet segmentations. Since PMSMs having fractional slot-to-pole number are very popular in the industries, we have chosen a three-phase, $12\,\text{s}/8\,\text{p}$, semi-closed, surface-mounted PMSM for our case study. The main parameters and dimensions of the PM motor are given in Table 1. The winding layout for the motor is graphically illustrated in Figure 4. Each phase winding consists of four coils which are located 90 deg. mech. apart. The phase windings are inherently symmetrical around the stator periphery, resulting in zero unbalanced magnetic pull. According to the analytical assessment reported in [14], it is observed that if one segmented magnet (1 SM) per pole is used under the radial magnetization pattern in the aforementioned machine, an optimum magnet pole-arc of 136.4° elect. can generate the peak cogging torque and THD_v of 0.19 Nm and 5.62%, respectively, as shown in Figure 5(a). Another important result in [14] indicates that the magnitude of the fundamental phase back-EMF is 19.09 V. Hence, assuming that similar total magnet volume is used, we deploy two segmented magnets (2 SM) per pole, and then analytically estimate the best segmented magnet pole-arcs by varying magnet spans of the virtual PM blocks, which can potentially lead to lower cogging torque and THD_v.

Figure 5(b) shows the trend of the normalized maximum cogging torque and normalized THD_v when the magnet span α_{p1} is changing from 136.4° elect. to one full pitch, which mutually corresponds to the change of magnet pole-arc α_{p2} from 0° elect. to 43.6° elect. From Figure 5(b), a considerably
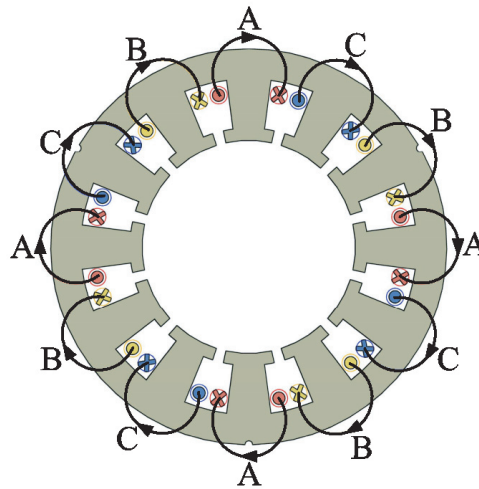

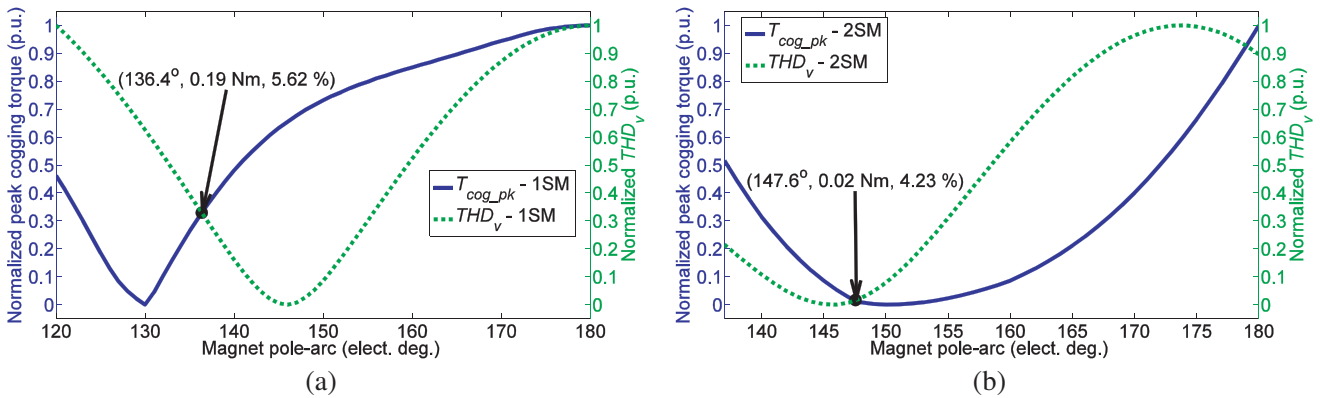**Figure 4.** Winding arrangement in a three-phase, $12\,\text{s}/8\,\text{p}$ PMSM.

Figure 5. Normalized peak cogging torque and normalized total harmonic distortion versus the magnet span variation in $12\,\text{s}/8\,\text{p}$ PMSMs with each magnetic pole of (a) $1\,\text{SM}$, (b) $2\,\text{SM}$.
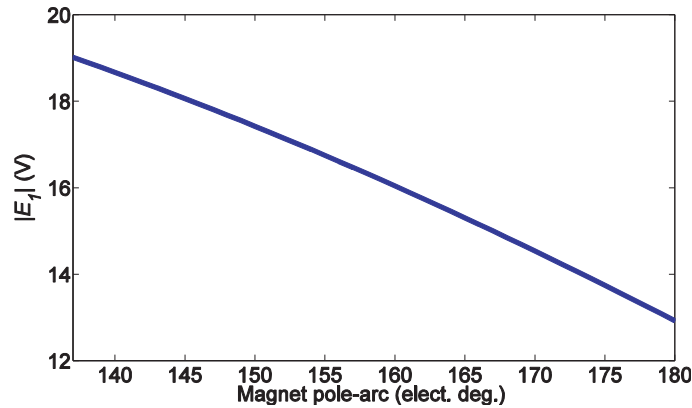

Figure 6. Fundamental phase back-EMF versus the magnet span variation in $12\,\text{s}/8\,\text{p}$ PMSM with $2\,\text{SM}$ per magnetic pole.

low cogging torque and THD_v of $0.02\,\text{Nm}$ and 4.23%, respectively, are attainable when α_{p1} is $147.6°$ elect. and α_{p2} is $11.2°$ elect. This is considered as the optimum setting for $2\,\text{SM}$ per pole in $12\,\text{s}/8\,\text{p}$ PM motor. Meanwhile, Figure 6 shows the variation of the phase back-EMF fundamental magnitude versus the magnet span α_{p1} in a $12\,\text{s}/8\,\text{p}$ PMSM with $2\,\text{SM}$ per pole. It indicates that the magnitude of fundamental phase back-EMF at the optimum setting of $2\,\text{SM}$ per pole is about $17.73\,\text{V}$. Comparing the analytical results obtained from $1\,\text{SM}$- and $2\,\text{SM}$ per pole motors, the cogging torque and THD_v have been significantly reduced by 89% and 25%, respectively.

The motor models were built and studied in 2-D FEA for comparison and validation purposes. Figure 7 exhibits the magnetic equipotential lines during open-circuit conditions in the $12\,\text{s}/8\,\text{p}$ PM machine with its optimum magnet pole-arc per pole for $1\,\text{SM}$ and $2\,\text{SM}$, respectively. The fields due to the magnet are slightly different in the airgap region by observing the field distributions in both machines. As can be seen in Figure 7(b), the airgap spacing that exists between magnet segments in the $2\,\text{SM}$ per pole machine is able to significantly nullify the pulling forces between PM interpoles and slot-openings, yielding a lower peak cogging torque. Figure 8 shows the radial and tangential components of magnetic flux density in the middle of airgap (at $r = 26.5\,\text{mm}$) in $12\,\text{s}/8\,\text{p}$ machines having similar total magnet volume with the optimum magnet pole-arcs in each magnetic pole for $1\,\text{SM}$ and $2\,\text{SM}$, respectively. The effect of stator slots can clearly be seen in the flux density distributions in both machines. As expected from this magnet segmentation, slightly higher magnitude of radial component of flux density is obtained in the $1\,\text{SM}$ per pole machine compared to that of $2\,\text{SM}$ per pole machine. Good agreement is achieved between the analytical results and FEA.

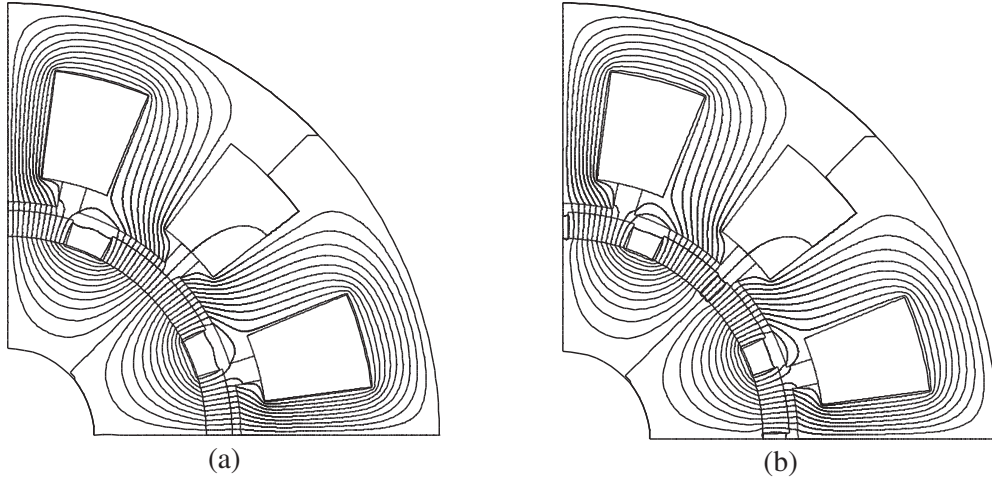**Figure 7.** Open-circuit magnetic field distributions predicted by FEA in $12\,\text{s}/8\,\text{p}$ PMSMs with its optimum magnet pole-arc per pole. (a) $1\,\text{SM}$. (b) $2\,\text{SM}$.
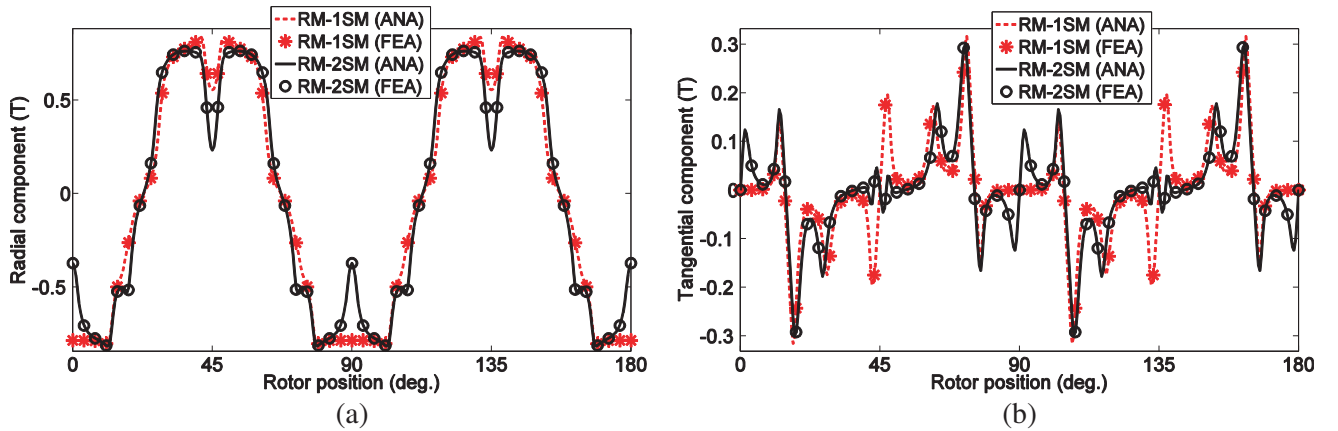

Figure 8. Open-circuit magnetic flux density in mid airgap ($r = 26.5\,\text{mm}$) of $12\,\text{s}/8\,\text{p}$ PMSMs having same PM volume with the optimum magnet pole-arcs in each magnetic pole of $1\,\text{SM}$ and $2\,\text{SM}$ predicted by analytical model and FE method. (a) Radial component. (b) Tangential component.

Figures 9 and 10 present the phase back-EMF and cogging torque waveforms in $12\,\text{s}/8\,\text{p}$ PMSMs which have similar total PM volume with the optimum magnet pole-arc in $1\,\text{SM}$ and $2\,\text{SM}$ per pole as predicted by analytical model and FEA. Clearly, the motor performance of both machines predicted by the analytical model and FE method show good agreements. As can be noted, the phase back-EMF generated by the $2\,\text{SM}$ per pole machine is marginally smaller than that of the $1\,\text{SM}$ per pole machine. This is because the magnitude of radial component of magnetic flux density in the $2\,\text{SM}$ per pole machine is marginally smaller than the $1\,\text{SM}$ per pole machine, as illustrated earlier in Figure 8(a). However, the $2\,\text{SM}$ per pole machine is inherently able to exhibit considerably smaller value of undesirable cogging torque as compared with that of $1\,\text{SM}$ per pole machine. Creating the airgap spacing between magnet segmentations in each magnetic pole provides similar effects as the dummy slots in the stator tooth surface.

Therefore, using this analytical subdomain method for searching and determining the optimum setting of the segmented magnet pole-arcs, more sinusoidal phase back-EMF is achievable, and the cogging torque can be minimized to a substantially low value as exemplified by the $2\,\text{SM}$ per pole machine in this case study. Lower values of THD_v and cogging torque are important design requirements for smooth output torque in PMSMs.
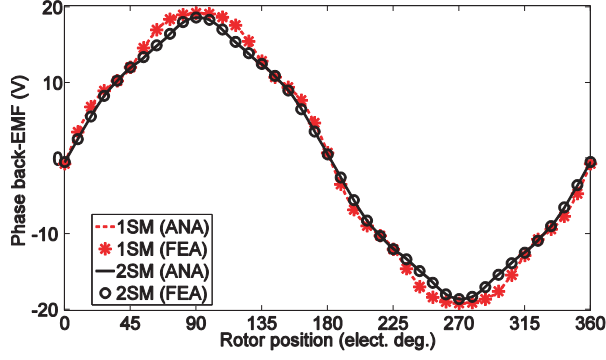
Figure 9. Phase back-EMF in 12 s/8 p PMSMs having the same PM volume with optimum magnet pole-arcs in each magnetic pole of 1 SM and 2 SM predicted by analytical model and FE method.

Figure 10. Cogging torque in 12 s/8 p PMSMs having same PM volume with optimum magnet pole-arcs in each magnetic pole of 1 SM and 2 SM predicted by analytical model and FE method.

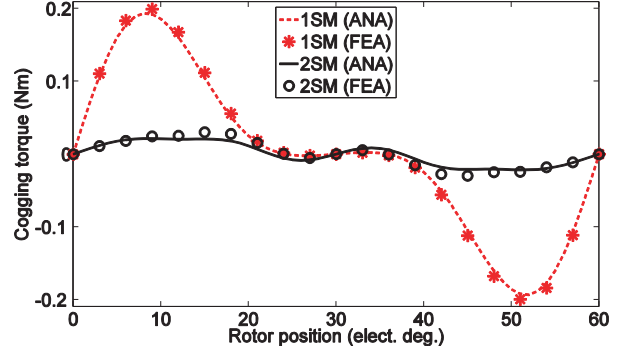## 6. CONCLUSIONS

An analytical subdomain model using virtual PM blocks to represent magnet segmentations in surface-mounted PMSMs has been described. The analytical model can be used to determine the optimum magnet pole-arc setting of segmented magnets under the influence of radial magnetization patterns. A generic machine of three-phase, 12 s/8 p surface-mounted PM motor has been selected with either 1 SM- or 2 SM per pole. The peak cogging torque and THD_v of phase back-EMF have been normalized by using the feature scaling method to determine their optimum settings. The optimum magnet pole-arc of 136.4° elect. for the 1 SM per pole machine is able to produce about 0.19 Nm of peak cogging torque, 5.62% of THD_v, and 19.09 V of the fundamental phase back-EMF, respectively. By imposing the same PM volume as a constraint, the optimum setting for 2 SM pole-arcs is found to be 147.6° elect. per pole associated with 11.2° elect. of airgap spacing between two magnet segments. The optimum 2 SM per pole machine is predicted to generate peak cogging torque, THD_v, and fundamental magnitude of phase back-EMF about 0.02 Nm, 4.23%, and 17.73 V, respectively. The optimum setting of the 2 SM per pole machine exhibits better performances as compared with those of the 1 SM per pole machine, where the cogging torque and THD_v have been reduced by 89% and 25%, respectively.

ACKNOWLEDGMENT

APPENDIX A.

All coefficients in the field solutions describing the vector magnetic potentials in each region, i.e., PM, airgap, slot-openings, and winding slots, can be estimated by applying the boundary conditions at the respective interfacing regions [13, 16, 18].

A.1. Interface between Airgap and PM

Since the normal component of flux density is continuous between airgap and PM at radius R_m, the following equations can be obtained

$$\left(1+G_1^2\right) A_1 - G_2 A_2 - B_2 = \begin{cases} -\dfrac{\mu_0}{(k^2-1)} \left[(R_r k G_1 + R_m) M_{\alpha ck} - (R_r G_1 + k R_m) M_{rsk}\right], & k \neq 1 \\ -\mu_0 \left[(2 R_r G_1 + R_m) M_{\alpha ck} - (R_r G_1 + R_m) M_{rsk}\right], & k = 1 \end{cases} \quad \text{(A1)}$$

$$\left(1+G_1^2\right)C_1 - G_2C_2 - D_2 = \begin{cases} -\dfrac{\mu_0}{(k^2-1)}\left[(R_rkG_1+R_m)\,M_{\alpha sk}+(R_rG_1+kR_m)\,M_{rck}\right], & k\neq 1 \\ -\mu_0\left[(2R_rG_1+R_m)\,M_{\alpha sk}+(R_rG_1+R_m)\,M_{rck}\right], & k=1 \end{cases} \tag{A2}$$

$$\left(1-G_1^2\right)A_1 - \mu_rG_2A_2 + \mu_rB_2 = \begin{cases} -\dfrac{\mu_0}{(k^2-1)}\left[k\,(R_m-R_rG_1)\,M_{\alpha ck}-(R_m-R_rG_1)\,M_{rsk}\right], & k\neq 1 \\ -\mu_0\left[2\,(R_m-R_rG_1)\,M_{\alpha ck}-(R_m-R_rG_1)\,M_{rsk}\right], & k=1 \end{cases} \tag{A3}$$

$$\left(1-G_1^2\right)C_1 - \mu_rG_2C_2 + \mu_rD_2 = \begin{cases} -\dfrac{\mu_0}{(k^2-1)}\left[k\,(R_m-R_rG_1)\,M_{\alpha sk}+(R_m-R_rG_1)\,M_{rck}\right], & k\neq 1 \\ -\mu_0\left[2\,(R_m-R_rG_1)\,M_{\alpha sk}+(R_m-R_rG_1)\,M_{rck}\right], & k=1 \end{cases} \tag{A4}$$

$$G_2 = (R_m/R_s)^k \tag{A5}$$

A.2. Interface between Slot Opening and Winding Slot

Similarly, applying the tangential component of flux density which is continuous at this interface in a non-overlapping machine, the following expressions can be obtained

$$B_{3i\alpha n} = B_{4i\alpha 0}\gamma_0 + \sum_m B_{4i\alpha m}\gamma \tag{A6}$$

$$A_{3t0} = D\ln R_t + Q_{4i} \tag{A7}$$

$$\sum_n A_{3in}\zeta = C_{4i} + D_{4i}G_4 \tag{A8}$$

where

$$B_{3i\alpha n} = -E_nD_{3i}\left(G_3^2-1\right)/R_t - 2\mu_0J_{in}\left(R_t^2-R_{sb}^2G_3\right)/\left[R_t\left(E_n^2-4\right)\right] \tag{A9}$$

$$B_{4i\alpha 0} = -D/2 \tag{A10}$$

$$D = \mu_0J_{i0}\left(b_{sa}/b_{oa}\right)\left(R_{sb}^2-R_t^2\right)/2 \tag{A11}$$

$$\gamma_0 = 4\cos\left(n\pi/2\right)\sin\left(E_nb_{oa}/2\right)/n\pi \tag{A12}$$

$$B_{4i\alpha m} = -F_m\left(C_{4i}-D_{4i}G_4\right)/R_t \tag{A13}$$

$$G_4 = (R_s/R_t)^{F_m} \tag{A14}$$

$$\gamma = \begin{cases} -2E_n/\left[b_{sa}\left(F_m^2-E_n^2\right)\right]\left[\cos\left(m\pi\right)\sin\left(E_n\{b_{sa}+b_{oa}\}/2\right)-\sin(E_n\{b_{sa}-b_{oa}\}/2)\right], & F_m\neq E_n \\ b_{oa}/b_{sa}\cos\left[F_m(b_{sa}-b_{oa})/2\right], & F_m = E_n \end{cases} \tag{A15}$$

$$A_{3t0} = \sum_n A_{3in}\zeta_0 + \mu_0J_{i0}\left(2R_{sb}^2\ln R_t - R_t^2\right)/4 + Q_{3i} \tag{A16}$$

$$A_{3in} = D_{3i}\left(G_3^2+1\right) + \mu_0J_{in}\left(R_t^2-2R_{sb}^2G_3/E_n\right)/\left(E_n^2-4\right) \tag{A17}$$

$$\zeta_0 = b_{sa}\gamma_0/(2b_{oa}) \tag{A18}$$

$$\zeta = b_{sa}\gamma/b_{oa} \tag{A19}$$

A.3. Interface between Airgap and Slot-Opening

The interface condition for the tangential component of flux density which is continuous between airgap and slot-opening produces solution sets as

$$-kA_2 + kG_2B_2 = R_sC_s \tag{A20}$$

$$-kC_2 + kG_2D_2 = R_sD_s \tag{A21}$$

$$G_4C_{4i} + D_{4i} = \sum_k \left(A_{2c}\sigma_i + A_{2s}\tau_i\right) \tag{A22}$$

$$\sum_k \left(A_{2c}\sigma_{i0} + A_{2s}\tau_{i0}\right) = D\ln R_s + Q_{4i} \tag{A23}$$

where

$$C_s = \sum_{i,m} B_{i\alpha m}\eta_i + \sum_i B_{i\alpha 0}\eta_{i0} \tag{A24}$$

$$D_s = \sum_{i,m} B_{i\alpha m}\xi_i + \sum_i B_{i\alpha 0}\xi_{i0} \tag{A25}$$

$$B_{i\alpha m} = -F_m \left(C_{4i} G_4 - D_{4i} \right) / R_s \tag{A26}$$

$$\eta_i = \begin{cases} -k / \left[\pi \left(F_m^2 - k^2 \right) \right] \left[\cos\left(m\pi \right) \sin\left(k\alpha_i + kb_{oa}/2 \right) - \sin\left(k\alpha_i - kb_{oa}/2 \right) \right], & F_m \neq k \\ b_{oa} \cos\left[F_m \left(\alpha_i - b_{oa}/2 \right) \right]/2\pi, & F_m = k \end{cases} \tag{A27}$$

$$\xi_i = \begin{cases} k / \left[\pi \left(F_m^2 - k^2 \right) \right] \left[\cos\left(m\pi \right) \cos\left(k\alpha_i + kb_{oa}/2 \right) - \cos\left(k\alpha_i - kb_{oa}/2 \right) \right], & F_m \neq k \\ b_{oa} \sin\left[F_m \left(\alpha_i - b_{oa}/2 \right) \right]/2\pi, & F_m = k \end{cases} \tag{A28}$$

$$B_{i\alpha 0} = -D/R_s \tag{A29}$$

$$\eta_{i0} = 2 \sin\left(kb_{oa}/2 \right) \cos\left(k\alpha_i \right)/(k\pi) \tag{A30}$$

$$\xi_{i0} = 2 \sin\left(kb_{oa}/2 \right) \sin\left(k\alpha_i \right)/(k\pi) \tag{A31}$$

$$A_{2c} = A_2 + G_2 B_2 \tag{A32}$$

$$A_{2s} = C_2 + G_2 D_2 \tag{A33}$$

$$\sigma_i = \begin{cases} 2\pi\eta_i/b_{oa}, & F_m \neq k \\ \cos\left(F_m \alpha_i - m\pi/2 \right), & F_m = k \end{cases} \tag{A34}$$

$$\tau_i = \begin{cases} 2\pi\xi_i/b_{oa}, & F_m \neq k \\ \sin\left(F_m \alpha_i - m\pi/2 \right), & F_m = k \end{cases} \tag{A35}$$

$$\sigma_{i0} = \pi\eta_{i0}/b_{oa} \tag{A36}$$

$$\tau_{i0} = \pi\xi_{i0}/b_{oa} \tag{A37}$$

REFERENCES

1. Bianchi, N., S. Bolognani, and F. Luise, "Potentials and limits of high-speed PM motors," *IEEE Trans. Ind. Appl.*, Vol. 40, 1570–1578, 2004.

2. Pfister, P. D. and Y. Perriard, "Very-high-speed slotless permanent-magnet motors: Analytical modeling, optimization, design, and torque measurement methods," *IEEE Trans. Ind. Electron.*, Vol. 57, 296–303, 2010.

3. Magnussen, F. and H. Lendenmann, "Parasitic effects in PM machines with concentrated windings," *IEEE Trans. Ind. Appl.*, Vol. 43, 1223–1232, 2007.

4. Valavi, M., A. Nysveen, R. Nilssen, R. D. Lorenz, and T. Rølvåg, "Influence of pole and slot combinations on magnetic forces and vibration in low-speed PM wind generators," *IEEE Trans. Magn.*, Vol. 50, 2014.

5. Islam, M. S., S. Mir, T. Sebastian, and S. Underwood, "Design considerations of sinusoidally excited permanent-magnet machines for low-torque-ripple applications," *IEEE Trans. Ind. Appl.*, Vol. 41, 955–962, 2005.

6. Jahns, T. M. and W. L. Soong, "Pulsating torque minimization techniques for permanent magnet AC motor drives-a review," *IEEE Trans. Ind. Electron.*, Vol. 43, 321–330, 1996.

7. Polinder, H. and M. J. Hoeijmakers, "Eddy-current losses in the segmented surface-mounted magnets of a PM machine," *IEE Proceedings — Electric Power Applications*, Vol. 146, 261–266, 1999.

8. Madina, P., J. Poza, G. Ugalde, and G. Almandoz, "Analysis of non-uniform circumferential segmentation of magnets to reduce eddy-current losses in SPMSM machines," *20th International Conference on Electrical Machines Proceedings 2012 (ICEM 2012)*, 79–84, 2012.

9. Belli, Z. and M. R. Mekideche, "Optimization of magnets segmentation for eddy current losses reduction in permanent magnets electrical machines," *8th International Conference and Exhibition on Ecological Vehicles and Renewable Energies 2013 (EVER 2013)*, 2013.

10. Lateb, R., N. Takorabet, and F. Meibody-Tabar, "Effect of magnet segmentation on the cogging torque in surface-mounted permanent-magnet motors," *IEEE Trans. Magn.*, Vol. 42, 442–445, 2006.

11. Ashabani, M. and Y. A. R. I. Mohamed, "Multiobjective shape optimization of segmented pole permanent-magnet synchronous machines with improved torque characteristics," *IEEE Trans. Magn.*, Vol. 47, 795–804, 2011.

12. Ghasemi, A., "Cogging torque reduction and optimization in surface-mounted permanent magnet motor using magnet segmentation method," *Electric Power Components and Systems*, Vol. 42, 1239–1248, 2014.

13. Tiang, T. L., D. Ishak, C. P. Lim, and M. K. M. Jamil, "A comprehensive analytical subdomain model and its field solutions for surface-mounted permanent magnet machines," *IEEE Trans. Magn.*, Vol 51, 1–14, 2015.

14. Tiang, T. L., D. Ishak, C. P. Lim, and M. Kamarol, "Analytical assessment of optimum magnet pole-arc for PMSM under influence of different magnetization patterns," *IEEE International Magnetics Conference 2015 (INTERMAG 2015)*, Beijing, China, 2015.

15. Rahideh, A. and T. Korakianitis, "Analytical magnetic field distribution of slotless brushless PM motors. Part 2: Open-circuit field and torque calculations," *IET Electric Power Applications*, Vol. 6, 639-651, 2012.

16. Wu, L. J., Z. Q. Zhu, D. Staton, M. Popescu, and D. Hawkins, "Analytical prediction of electromagnetic performance of surface-mounted PM machines based on subdomain model accounting for tooth-tips," *IET Electric Power Applications*, Vol. 5, 597–609, 2011.

17. Rahideh, A., H. Moayed-Jahromi, M. Mardaneh, F. Dubas, and T. Korakianitis, "Analytical calculations of electromagnetic quantities for slotted brushless machines with surface-inset magnets," *Progress In Electromagnetics Research B*, Vol. 72, 49–65, 2017.

18. Lubin, T., S. Mezani, and A. Rezzoug, "2-D exact analytical model for surface-mounted permanent-magnet motors with semi-closed slots," *IEEE Trans. Magn.*, Vol. 47, 479–492, 2011.